Detection of local vibrational modes induced by intrinsic defects in undoped BaSi$_2$ light absorber layers using Raman spectroscopy

Takuma Sato, Hirofumi Hoshida, Ryota Takabe, Kaoru Toko, Yoshikazu Terai, and Takashi Suemasu

---

Articles you may be interested in

Theoretical efficiency of hybrid solar thermoelectric-photovoltaic generators
Journal of Applied Physics **124**, 024501 (2018); 10.1063/1.5022569

Enhanced irradiance sensitivity of 4H-SiC based ultraviolet sensor introducing laterally gated Al/SiO$_2$/SiC tunnel diode structure with low gate bias
Journal of Applied Physics **124**, 024503 (2018); 10.1063/1.5044678

A full-field crystal plasticity study on how texture and grain structure influences hydrostatic stress in thermally strained β-Sn films
Journal of Applied Physics **124**, 025302 (2018); 10.1063/1.5029933

On the method of photoconductive detection of defects in semiconductors by vibrational mode-related Fano resonances
Journal of Applied Physics **124**, 025704 (2018); 10.1063/1.5037412

Thermal conductivity, electrical resistivity, and dimensionless figure of merit (ZT) determination of thermoelectric materials by impedance spectroscopy up to 250 °C
Journal of Applied Physics **124**, 025105 (2018); 10.1063/1.5036937

Investigation of the retention performance of an ultra-thin HfO$_2$ resistance switching layer in an integrated memory device
Journal of Applied Physics **124**, 024102 (2018); 10.1063/1.5033967

Detection of local vibrational modes induced by intrinsic defects in undoped BaSi$_2$ light absorber layers using Raman spectroscopy

Takuma Sato,[1] Hirofumi Hoshida,[2] Ryota Takabe,[1] Kaoru Toko,[1] Yoshikazu Terai,[2] and Takashi Suemasu[1]

[1]*Institute of Applied Physics, University of Tsukuba, Tsukuba, Ibaraki 305-8573, Japan*
[2]*Department of Computer Science and Electronics, Kyushu Institute of Technology, Iizuka, Fukuoka 820-8502, Japan*

We fabricate BaSi$_2$ epitaxial films on Si(111) substrates by molecular beam epitaxy and investigate point defects inside the films using Raman spectroscopy with the help of first-principles calculation. Point defects such as Ba substituted for Si antisites, Si vacancies, and Si interstitials are considered as candidates for native point defects in BaSi$_2$. Vibration analysis based on first-principles calculation suggests that local vibrational modes caused by these point defects appear at around 430, 480, and 560 cm^{-1}, respectively, and are in good agreement with Raman peak positions. Comparing calculations with Raman spectra of the films formed with different Ba to Si deposition rate ratios R_{Ba}/R_{Si} from 1.0 to 5.1, we conclude that the density of point defects reaches a minimum at $R_{Ba}/R_{Si} = 2.2$. Furthermore, the position of Raman peaks at approximately 490 cm^{-1} shifts to a lower wavenumber, depending on R_{Ba}/R_{Si} and thereby the density of point defects. *Published by AIP Publishing.* https://doi.org/10.1063/1.5029320

I. INTRODUCTION

At present, wafer-based silicon (Si) solar cells have approximately 90% of the market share, and their conversion efficiency (η) has exceeded 26%.[1] The achieved η is already very close to the theoretical limit.[2] Hence, there is little room for further improvement in η. Under these situations, various materials have been studied as candidates for novel solar cells as a solution to future energy demand.[3–6] Among these materials, we have paid special attention to barium disilicide (BaSi$_2$) consisting of earth-abundant Ba and Si.[7] BaSi$_2$ possesses an indirect bandgap of 1.3 eV, which is more suitable than crystalline Si for a single-junction solar cell. Recent experiments have revealed that BaSi$_2$ has a sufficiently large minority-carrier diffusion length ($L \sim 10 \, \mu m$) and a large minority-carrier lifetime ($\tau \sim 10 \, \mu s$) for thin-film solar cells.[8–11] In addition, BaSi$_2$ has high absorption coefficients exceeding 3×10^4 cm^{-1} at 1.5 eV,[12] since its direct transition edge is located higher by only 0.1 eV than the bandgap.[13–16] Thus, η exceeding 25% is expected by utilizing outstanding properties of BaSi$_2$ for the light absorber layers in thin-film solar cells.[17] As BaSi$_2$ can be grown epitaxially on Si substrates[18] and its bandgap can be increased by adding other elements like Sr and C,[19,20] BaSi$_2$ is a material of choice for targeting $\eta > 30\%$ in a Si-based tandem solar cell. We have achieved η approaching 10% in p-BaSi$_2$/n-Si heterojunction solar cells[21,22] and recently demonstrated the operation of BaSi$_2$ homojunction solar cells.[23] BaSi$_2$ thin films have been grown by various methods[7] such as molecular beam epitaxy (MBE) using solid Si and Ba sources,[24] vacuum evaporation using BaSi$_2$ granules,[25] and radio-frequency sputtering using a BaSi$_2$ target.[26] Among them, vacuum evaporation and sputtering are practical methods for large-area solar cells, while MBE is more suitable to study the fundamental physical properties of BaSi$_2$.

Currently, we have been focusing our research on further improvement in minority-carrier properties of BaSi$_2$ absorber layers grown by MBE. Among them, photoresponsivity is a decisive parameter which significantly affects η. According to our previous work,[27] the photoresponsivity of 500-nm-thick undoped BaSi$_2$ films is fairly sensitive to the Ba to Si deposition rate ratios (R_{Ba}/R_{Si}) during the MBE growth and reached a maximum at around $R_{Ba}/R_{Si} = 2.2$ (Fig. 1). When R_{Ba}/R_{Si} is deviated from 2.2, the photoresponsivity decreases significantly. In these samples, we confirmed by Rutherford backscattering spectrometry (RBS) that the Ba to Si atomic ratios vary with R_{Ba}/R_{Si}.[27] We attribute these results to silicon vacancies (V$_{Si}$) forming localized states within the bandgap and thus working as recombination centers for photogenerated carriers. The first-principles calculation by Kumar *et al.*[28] suggested that native point defects including V$_{Si}$ form localized states within the bandgap of
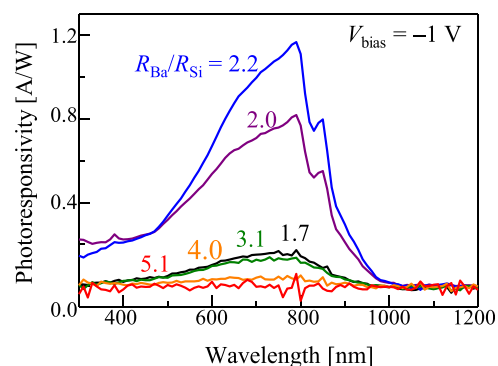
FIG. 1. Photoresponse spectra of 500-nm-thick BaSi$_2$ grown with various R_{Ba}/R_{Si} values measured under a bias voltage of -1 V applied to the front ITO electrode with respect to the back Al electrode. Reprinted with permission from Takabe *et al.*, J. Appl. Phys. **123**, 045703 (2018). Copyright 2018 AIP Publishing LLC.[27]

$BaSi_2$. Actually, we have detected electrically active defect levels in $BaSi_2$ films by deep-level transient spectroscopy (DLTS).[29–31] In DLTS, however, we need to form a junction to expand the depletion layer towards the region, where defects exist. In contrast to DLTS, there is no such restriction in Raman spectroscopy. In addition, Raman spectroscopy enables us to access the atomic structure of defects in $BaSi_2$ with the help of first-principles calculation because vibrational frequencies are specific to a molecule's chemical bonding and symmetry. There have been several defect studies using Raman spectroscopy such as Se vacancies in Cu(In, Ga)Se_2 and Si precipitations in β-$FeSi_2$ films.[32,33] However, there has been no such discussion about defects in $BaSi_2$ although there have been several reports on Raman spectra of $BaSi_2$ from both experimental and theoretical viewpoints so far.[34–37]

In this work, we first estimate residual stresses in the a-axis-oriented $BaSi_2$ epitaxial films grown on a Si(111) substrate based on the lattice constants deduced from x-ray diffraction measurements. This is to qualitatively understand the shift of the Raman peak position and discuss their origins. We next calculate the wavenumber of phonons in $BaSi_2$ possessing point defects introduced at the Γ point using the first-principles calculation and compare them with experiment.

II. EXPERIMENTAL METHODS

An ion-pumped MBE system equipped with an electron-beam evaporation source for Si and a standard Knudsen cell for Ba was used for the growth. Before growth, Czochralski (CZ) n-Si(111) (resistivity $\rho = 0.01\ \Omega$ cm) substrates were first cleaned according to standard RCA (Radio Corporation of America) procedure, followed by thermal cleaning at 900 °C for 30 min in the ultra-high vacuum chamber to remove a protective oxide layer on the surface. We then deposited Ba on a Si substrate heated at 500 °C by reactive deposition epitaxy to form a 3-nm-thick $BaSi_2$ template layer.[38] This template acts as a seed crystal for the subsequent layer. Subsequently, we grew approximately 600-nm-thick undoped $BaSi_2$ on the templates at 580 °C by MBE.[24] In order to investigate the relationship between R_{Ba}/R_{Si} and Raman peak positions, R_{Si} was fixed at 0.9 nm/min and R_{Ba} was varied from 0.9 to 4.6 nm/min during the MBE growth, meaning that R_{Ba}/R_{Si} was varied from 1.0 to 5.1. We then formed a 3-nm-thick amorphous Si layer at 180 °C, which works as a surface passivation layer for ensuring a good electrical contact.[11,39,40] Out-of-plane (θ–2θ) and in-plane (φ–$2\theta_\chi$) x-ray diffraction (XRD) measurements with a Cu Kα radiation source were performed to determine the lattice constants using the Nelson–Riley equation.[41] Raman spectra were measured with a laser Raman spectrometer (JASCO, NRS-5100) using a frequency doubled Nd:YAG laser (532 nm) at room temperature (RT). The time of acquisition for each Raman spectrum was 100 s. The absolute Raman shift was corrected by the transverse optical (TO) phonon line (520.2 cm^{-1}) of crystalline Si. In order to make assignment of local vibrational modes (LVM), polarized Raman spectra were also measured at the $X(YZ)\overline{X}$ geometry

of the typical Porto notation using a polarizer. The X-axis was parallel to $BaSi_2$[100]. In the $X(YZ)\overline{X}$ geometry, the Raman intensity of the A_g mode at around 490 cm^{-1} can be suppressed since there are only the diagonal components in the Raman tensor of the A_g mode.[42] So, we can expect that LVM at around 490 cm^{-1} is observed in the $X(YZ)\overline{X}$ geometry.

The crystal structure of orthorhombic $BaSi_2$ ($Z = 8$) is shown in Fig. 2. $BaSi_2$ belongs to the *Pnma* space group, and its unit cell contains eight formula units. The stoichiometric description of the unit cell is Ba_8Si_{16}. In the unit cell of $BaSi_2$, there are two crystallographically inequivalent sites for Ba [Ba(1) and Ba(2)] and three inequivalent sites for Si [Si(3), Si(4), and Si(5)]. In addition, there are four distinct Si tetrahedra with varying directions and positions that can be mutually translated by symmetric operations. In each Si tetrahedron, the two Si(5) atoms (blue spheres in Fig. 2) and the single Si(4) atom (red sphere in Fig. 2) have similar a-axis coordinates. Two intrinsic point defects, Si vacancy (V_{Si}) and Ba substituted for Si antisites (Ba_{Si}), were introduced into one of the four Si(3) sites as previously reported.[27,28] We adopted a previously reported interstitial site, the fractional coordinate of which is (0.5841, 0.25, 0.2251), as an initial configuration for Si interstitials (Si_i).[43,44] The vibrational frequency calculation at the Γ point was performed with QUANTUM ESPRESSO code[45] within the framework of *ab initio* pseudopotential density functional perturbation theory.[46] We employed the norm-conserving pseudopotentials with generalized gradient approximation in Troullier-Martins type,[47] and the cut-off energy of the plane-wave basis sets was 45 Ry. For k points in the Brillouin zone, a $3 \times 4 \times 2$ Monkhorst-Pack mesh was used for a perfect crystal (with an orthorhombic cell). The estimated energy error in self-consistency was less than 10^{-14} a.u. Relaxation was performed until the total energy changed by less than 10^{-5} a.u., and the components of forces were smaller than 10^{-4} a.u. during geometry optimization.

III. RESULTS AND DISCUSSION

A. Lattice constants and residual stress

The peak shift of the Raman spectrum $\Delta\omega$ is proportional to the magnitude of the residual stress σ_{res} in the film.[48,49] Hence, we estimate σ_{res} by using lattice constants
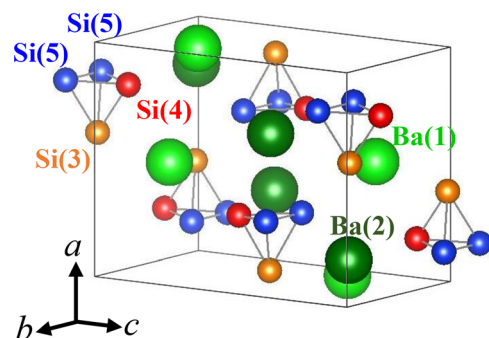

FIG. 2. Crystal structure of $BaSi_2$ ($Z = 8$). There are two crystallographically inequivalent sites for Ba [Ba(1) and Ba(2)] and three inequivalent sites for Si [Si(3), Si(4), and Si(5)] in the orthorhombic unit cell of $BaSi_2$.

of the *a*-axis-oriented undoped $BaSi_2$ epitaxial film. The lattice constants as a function of R_{Ba}/R_{Si} are shown in Fig. 3. We calculate the lattice constants from the XRD peak positions obtained from out-of-plane (*a*) and in-plane (*b* and *c*) XRD patterns by using the Nelson-Riley relationship.[41] As can be seen in Fig. 3, *a* becomes larger as R_{Ba}/R_{Si} increases and then decreases with a further increase in R_{Ba}/R_{Si} after reaching a maximum in the vicinity of 2.2. On the other hand, *b* and *c* show the tendency opposite to *a*. From the obtained lattice constants, we evaluate the strain ε_{ii} in the directions of *a*, *b*, and *c* based on the following equation:

$$\varepsilon_{ii} = \frac{d_{(hkl)} - d_{0(hkl)}}{d_{0(hkl)}} \quad (i = 1, 2, 3), \quad (1)$$

where $d_{(hkl)}$ is the measured lattice spacing of $BaSi_2$ and $d_{0(hkl)}$ is the lattice spacing of unstrained $BaSi_2$. As the lattice constants of the relaxed sample, those of powdered XRD are used.[50] Following Hooke's law, the residual stress in the film is obtained from the evaluated strain as

$$\sigma_{ij} = S_{ijkl}\,\varepsilon_{kl} \quad (i, j, k, l = 1, 2, 3), \quad (2)$$

where s_{ijkl} are the compliance constants of single crystal $BaSi_2$, and the values calculated by Peng *et al.* are used for them.[35] Evaluation of the residual stress in the film by XRD is carried out assuming an in-plane stress condition ($\sigma_{11} = \sigma_{12} = \sigma_{13} = 0$) as applied to, for example, $\langle 111 \rangle$-oriented Al thin films on a Si(001) substrate.[51] However, in this work, it was difficult to obtain diffractions of sufficient intensity from the asymmetric planes of $BaSi_2$. Hence, diffractions such as (0*k*0) and (00*l*) obtained in the in-plane XRD measurement were used. The stress σ_{22} ($\parallel \sigma_b$) and σ_{33} ($\parallel \sigma_c$) in the plane were roughly estimated by assuming that the principal axes of stress coincided with the crystal axes. Figure 4(a) shows the result of the calculated strain ε_{11} ($= \varepsilon_a$) in the direction perpendicular to the film from the obtained in-plane stress using Eq. (2). The R_{Ba}/R_{Si} dependence of the

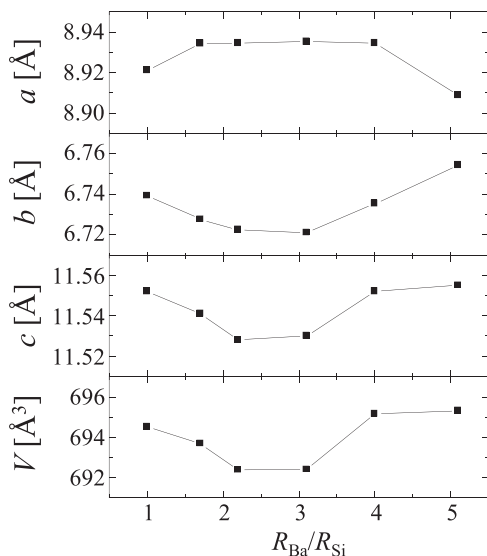*a*-axis lattice constant of the $BaSi_2$ film on Si(111) can be qualitatively understood by the above model, that is, the in-plane stress model assumed the principal axes of stress coincides with the crystal axes. On the other hand, the residual stress σ_{res} in the film is expressed by the sum of thermal stress σ_{th}, intrinsic stress σ_{int}, and external stress σ_{ext} given by

$$\sigma_{res} = \sigma_{th} + \sigma_{int} + \sigma_{ext}. \quad (3)$$

Using the following equation, we calculate the thermal stress:

$$\sigma_{th} = \frac{E_f}{1 - v_f}(\alpha_f - \alpha_s)\Delta T, \quad (4)$$

where α_s and α_f are the linear thermal expansion coefficients of Si and $BaSi_2$, and ΔT is the difference between the Si substrate temperature during MBE growth and room temperature. E_f and ν_f are the Young's modulus and Poisson's ratio of $BaSi_2$, respectively. We employ the values of 50 GPa and 0.201[52] for them, respectively. Figure 4(b) shows that the R_{Ba}/R_{Si} dependence of the intrinsic stress σ_{int} subtracted the thermal stress σ_{th} from the in-plane residual stress σ_{res}. σ_b and σ_c are the intrinsic stresses in the *b*-axis and *c*-axis directions, respectively, assuming the external stress $\sigma_{ext} = 0$. Intrinsic stress is caused by extinction of point defects and/or vacancies,[53] formation of grain boundaries,[54] and interface lattice mismatch between the substrate and the film.[54,55] There is not so much difference in the effect of grain boundary and lattice mismatch among the $BaSi_2$ films grown with different R_{Ba}/R_{Si} values. Therefore, we consider that the contribution of defects in undoped $BaSi_2$ films is mainly responsible for the variation of intrinsic stress on R_{Ba}/R_{Si}.

B. Calculation results

In order to discuss the effects of point defects mentioned in Sec. III A on the Raman spectrum, we calculate the vibrational frequencies of $BaSi_2$ including point defects by the first-principles calculation. First, we confirm the reproducibility of this calculation. Table I shows the calculation results of the Raman active modes at the Γ point [$q = (0,0,0)$] in a $BaSi_2$ perfect crystal. The relative magnitudes of displacement of the Si_4 cluster and Ba for each mode are also shown. As reported previously by Peng *et al.*,[35] lattice vibrations of Ba atoms are hardly observed at wavenumbers higher than $200\,cm^{-1}$, and all the calculated
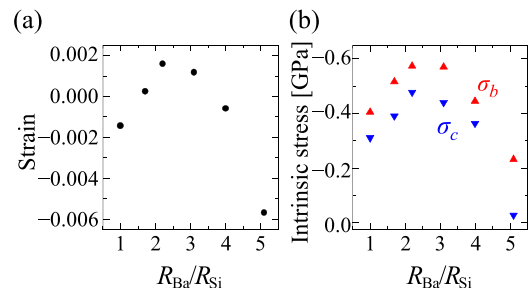

FIG. 3. Lattice constants (*a*, *b*, and *c*) and a unit cell volume (*V*) as a function of R_{Ba}/R_{Si} for 600-nm-thick undoped $BaSi_2$ films.

FIG. 4. (a) Strain in the *a*-axis direction and (b) intrinsic stress in the *b*-axis and *c*-axis directions as a function of R_{Ba}/R_{Si}.

TABLE I. Calculated Raman active optical phonon frequencies (cm^{-1}) of BaSi$_2$ at the Γ point. The modes are categorized to external modes (ext) including the translation of the Si cluster (t) and rotation of that (r), internal modes of the Si cluster (int), and the modes of Ba. Their relative magnitudes of displacement are also shown as vs = very strong, s = strong, m = medium, and w = weak.

Freq. (cm^{-1})	Si		Ba	Freq. (cm^{-1})	Si		Ba
51.2	ext	m	s	134.7	ext(t,r)	s	…
52.7	ext	s	vs	141.0	ext(r)	s	w
63.4	ext(t)	s	vs	145.5	ext(t,r)	vs	w
64.1	ext(t,r)	m	s	149.8	ext(r)	vs	w
66.2	ext(t,r)	m	vs	154.8	ext(r)	vs	w
71.0	ext(r)	m	s	156.7	ext(r)	vs	m
71.7	ext(t,r)	m	s	267.9	int	s	…
73.3	ext(t,r)	w	vs	268.9	int	s	…
75.8	ext(t)	s	vs	282.3	int	vs	…
75.9	ext(r)	m	vs	286.7	int	vs	…
82.0	ext(t,r)	s	vs	361.0	int	vs	…
93.9	ext(r)	m	vs	362.0	int	vs	…
103.3	ext(r)	vs	w	364.6	int	vs	…
113.2	ext(r)	vs	-	365.1	int	vs	…
118.9	ext(t,r)	s	w	384.9	int	vs	…
124.1	ext(r)	s	w	387.6	int	vs	…
127.8	ext(t,r)	vs	W	499.8	int	vs	…
130.6	ext(t,r)	vs	W	502.5	int	vs	…

modes are internal vibrations of Si$_4$ clusters. On the other hand, the modes observed below 200 cm^{-1} are the external vibrations (rotation and translation) of the Si$_4$ clusters and/or the lattice vibrations of Ba. For comparison, Table II summarises the Raman peak positions due to a Si$_4$ cluster in BaSi$_2$ by experiment[34,36,37] and by calculation.[35] Terai *et al.* also pointed out such a feature of modes in the measurement of the angle dependencies of polarized Raman spectra of *a*-axis-oriented undoped BaSi$_2$ epitaxial films on Si(001).[37] Comparing the present calculated peak positions of Raman active modes to the experimental result in powdered BaSi$_2$,[34] we confirm that the peak positions are almost reproducible. In particular, with respect to the internal vibrations of Si$_4$ cluster, the reproductivity is within ± 2–3%. In Raman scattering experiments, the A$_g$ modes at around 500 cm^{-1} as shown in Fig. 5 are the most intense peak. Hereafter, we pay attention to the A$_g$ modes of each sample.

We next investigated the effect of point defects in BaSi$_2$ on the Raman peak position. Based on the report by Kumar *et al.*,[28] we adopted three native defects such as

TABLE II. Raman peak positions due to a Si$_4$ cluster in BaSi$_2$ reported in Refs. 34–37. They are based on the results of powdered BaSi$_2$,[34] phonon density of states (DOS),[35] BaSi$_2$ film on Si(001) by vacuum evaporation,[36] and BaSi$_2$ film on Si(001) by MBE.[37]

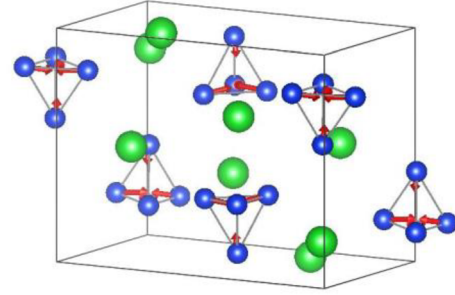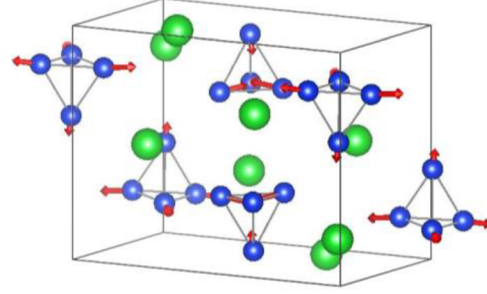| Powdered BaSi$_2$[34]	Phonon DOS[35]	BaSi$_2$/Si(001)[36]	BaSi$_2$/Si(001)[37]
276	282	278	280
293	296	292	295
355	…	355	358
…	363	…	362
376	381	376	380
486	486	486	486

(a) 499.8 cm^{-1}

(b) 502.5 cm^{-1}

FIG. 5. Schematics of Raman active A$_g$ modes calculated at the Γ point in a BaSi$_2$ perfect crystal at (a) 499.8 cm^{-1} and (b) 502.5 cm^{-1}.

V$_{Si}$, Ba$_{Si}$, and Si$_i$. As shown in Fig. 1, BaSi$_2$ has three crystallographically inequivalent Si sites in the unit cell; Si(3) and Si(4) occupy the 4c site, and Si(5) occupies the 8d site. Table III shows the calculated total energy of compounds including one vacancy (Ba) into each Si site, which is described as Ba$_8$Si$_{15}$V$_{Si(3)}$, Ba$_8$Si$_{15}$V$_{Si(4)}$, and Ba$_8$Si$_{15}$V$_{Si(5)}$ (Ba$_8$Si$_{15}$Ba$_{Si(3)}$, Ba$_8$Si$_{15}$Ba$_{Si(4)}$, and Ba$_8$Si$_{15}$Ba$_{Si(5)}$). From the viewpoint of total energy, both V$_{Si}$ and Ba$_{Si}$ seem to be easily introduced into the Si(3) site. This trend is consistent with previous reports.[27,28] On the other hand, there are 16 sites into which interstitial impurities can be introduced. According to Imai and Watanabe,[44] the most probable insertion sites are the 4c sites, where an impurity atom is surrounded by three Si atoms, one of which is at a peak of one Si-tetrahedron and the other two of which are composed of an angle of the other Si-tetrahedron. Thus, we employed one of the 4c sites as the initial configuration of Si$_i$, the fractional coordinate of which is (0.5841, 0.25, 0.2251). Table IV shows the initial configurations of the three native point defects used to calculate the vibrational frequencies. Interstitial oxygen (O$_i$) is also included in Table IV for later discussion. The calculated phonon

TABLE III. Calculated total energies [Ry] for compounds. V$_{Si}$ or Ba$_{Si}$ is introduced into one of the crystallographically inequivalent Si sites in the unit cell.

Compounds	Total energy
Ba$_8$Si$_{15}$V$_{Si(3)}$	−139.97
Ba$_8$Si$_{15}$V$_{Si(4)}$	−139.95
Ba$_8$Si$_{15}$V$_{Si(5)}$	−139.96
Ba$_8$Si$_{15}$Ba$_{Si(3)}$	−142.33
Ba$_8$Si$_{15}$Ba$_{Si(4)}$	−142.20
Ba$_8$Si$_{15}$Ba$_{Si(5)}$	−142.25

TABLE IV. Fractional coordinates of three intrinsic defects as an initial configuration.

Intrinsic defects	Fractional coordinates		
	x	y	Z
Si vacancy $V_{Si(3)}$	0.424	0.25	0.091
Ba antisite $Ba_{Si(3)}$	0.424	0.25	0.091
Si interstitial Si_i	0.5841	0.25	0.2251
O interstitial O_i	0.5841	0.25	0.2251

frequencies of A_g modes are shown in Table V together with that of perfect crystal. We predict the local vibrational modes shown in Figs. 6(a)–6(c) to emerge at certain wavenumbers presented in bold in Table V. The appearance of local vibrational modes by the introduction of point defects has been confirmed by Raman spectroscopy, for example, in B doped bulk Si.[56] On the other hand, as shown in Table V, the peak position of the main peak (A_g mode) shown in Fig. 5 is expected to shift to lower wavenumbers because of the formation of native defects.

C. Effects of native defects on the Raman Spectrum

Based on the discussions in Secs. III A and III B, we attempted to detect native defects by Raman spectroscopy in undoped $BaSi_2$ with different R_{Ba}/R_{Si}. Figure 7 shows the Raman spectra of undoped $BaSi_2$ in the range between 200 and 650 cm^{-1} at RT. Peaks due to the internal vibration of the Si_4 cluster can be observed at wavenumbers ranging from 250 to 500 cm^{-1}. The Raman lines originate from Si tetrahedra with T_h symmetry in the lattice of $BaSi_2$. In the past, they were assigned based on Si tetrahedra with T_d symmetry;[34,36,37] however, we found very recently that T_h symmetry is more suitable on the basis of experiments by polarized Raman spectroscopy and by infrared absorption spectroscopy. Besides, the Si–Si distances within each Si tetrahedron are different as in 0.234, 0.237, 0.237, 0.241, 0.248, and 0.248 nm,[57] meaning that T_d symmetry is not valid. Details will be reported elsewhere.

Figure 8(a) presents an enlarged view of the main peak due to the A_g mode at approximately 490 cm^{-1}. Figure 8(b) shows a plot of the peak wavenumber of the Ag mode in Fig. 8(a) against R_{Ba}/R_{Si}, showing that it reaches a maximum in the vicinity of $R_{Ba}/R_{Si} = 2.2$. From the calculation results in Sec. III B, it is expected that the shift of this main peak to a lower wavenumber is ascribed to the influence of native defects.

TABLE V. Calculated phonon frequencies of Raman active A_g modes of perfect crystal (Ba_8Si_{16}) and defective crystals such as $Ba_8Si_{15}V_{Si(3)}$, $Ba_8Si_{15}Ba_{Si(3)}$, $Ba_8Si_{16}Si_i$, and $Ba_8Si_{16}O_i$. Frequencies in boldface are local vibrational modes (LVM).

Ba_8Si_{16}	$Ba_8Si_{15}V_{Si(3)}$	$Ba_8Si_{15}Ba_{Si(3)}$	$Ba_8Si_{16}Si_i$	$Ba_8Si_{16}O_i$
499.8	469.5	**436.8 (LVM)**	442.7	447.2
502.5	474.1	457.1	465.7	478.7
	477.1	472.1	477.1	484.7
	477.7 (LVM)	486.6	**556.7 (LVM)**	**597.3 (LVM)**

(a) V_{Si} 477.7 cm^{-1}

(b) Ba_{Si} 436.8 cm^{-1}

(c) Si_i 556.7 cm^{-1}
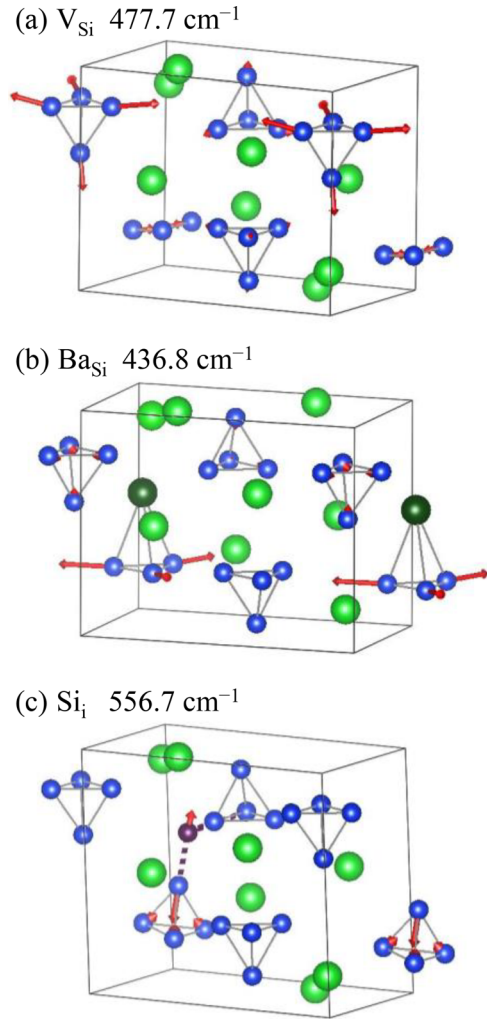
FIG. 6. Schematics of local vibrational modes of (a) V_{Si}, (b) Ba_{Si}, and (c) Si_i.

Therefore, the shift of the main peak was examined from the viewpoint of the atomic ratio of Ba to Si, N_{Ba}/N_{Si}, in these samples. Using the depth profile of N_{Ba}/N_{Si} obtained by RBS,[27] we calculated N_{Ba}/N_{Si} in the film surface weighted by
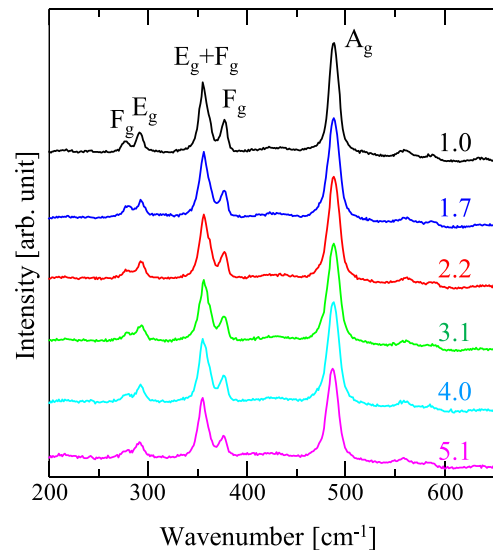
FIG. 7. Raman spectra of 600-nm-thick undoped $BaSi_2$ films with different R_{Ba}/R_{Si} values in the range of 200–650 cm^{-1} at RT.

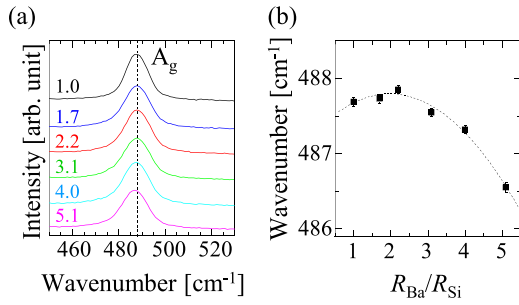FIG. 8. (a) Raman spectra of 600-nm-thick undoped BaSi$_2$ films with different R_{Ba}/R_{Si} values in the range of 450–530 cm^{-1} at RT. (b) A main peak (A$_g$ mode) position in (a) as functions of R_{Ba}/R_{Si}.

the optical absorption coefficient of BaSi$_2$ at a wavelength of the incident light $\lambda = 532$ nm used in this Raman measurement

$$\frac{N_{Ba}}{N_{Si}} = \frac{\int N_{RBS}(z)e^{-\alpha Z}dz}{\int e^{-\alpha Z}dz}, \tag{5}$$

where $N_{RBS}(z)$ is the measured N_{Ba}/N_{Si} at a depth z by RBS, and $\alpha = 3 \times 10^5$ cm^{-1} is used as the light absorption coefficient at $\lambda = 532$ nm. Substituting these values for Eq. (5), we calculated the weighted N_{Ba}/N_{Si} values to be 0.477, 0.499, and 0.510 for $R_{Ba}/R_{Si} = 1.0$, 2.2, and 4.0, respectively. Figure 9 plots the peak position of A$_g$ mode of the present Raman spectra against weighted N_{Ba}/N_{Si}. From the viewpoint of stoichiometry, we consider that native point defects in the film are least abundant at $R_{Ba}/R_{Si} = 2.2$ because it is the closest to stoichiometry ($N_{Ba}/N_{Si} = 0.5$). Thus, the main peak shift in Fig. 8(b) is considered to reflect the influence of native point defects. In order to further confirm the validity of this interpretation, we discuss the appearance of local vibrational modes accompanying the formation of native defects shown in Figs. 6(a)–6(c).

First, we examine V$_{Si}$, which is most likely to occur according to Kumar *et al.*[28] Although the local vibrational mode of V$_{Si}$ is expected to appear at approximately 480 cm^{-1}, it is very close to the peak position of the most intense peak of the A$_g$ mode. Figure 10 shows the full width at half maximum (FWHM) of the peak intensity of Ag mode as a function of R_{Ba}/R_{Si}. The FWHM value increased with R_{Ba}/R_{Si}. Polarized Raman spectra measured at RT on samples prepared with

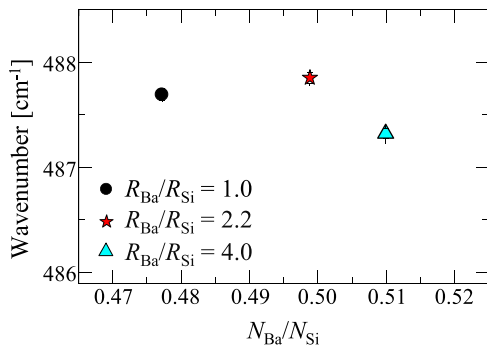$R_{Ba}/R_{Si} = 1.0$ and 5.1 are also shown. One Lorentzian curve located at around 486 cm^{-1} is enough to reconstruct the measured spectrum at $R_{Ba}/R_{Si} = 1.0$. However, another Lorentzian curve located at around 480 cm^{-1} is necessary to reconstruct the experimental data at $R_{Ba}/R_{Si} = 5.1$. As the contribution of this peak increases with R_{Ba}/R_{Si}, this peak is assumed to originate from V$_{Si}$. We thus speculate that the number of V$_{Si}$ increases with R_{Ba}/R_{Si}. Further analyses using the positron annihilation method, which is sensitive to vacancies, help us further confirm the validity of this interpretation.

Figure 11 presents the highlighted Raman spectra of BaSi$_2$ films with different R_{Ba}/R_{Si} values. Additional peaks denoted by broken lines at 430, 560, and 590 cm^{-1} are observed. Figure 12 presents the R_{Ba}/R_{Si} dependence of the peak intensity at 430 cm^{-1} normalized using the A$_g$ mode intensity at 490 cm^{-1}. The dotted lines are guides to the eye. The peak intensity increases with increasing R_{Ba}/R_{Si}. In addition, the calculated phonon frequency caused by the vibrational mode of Ba$_{Si}$ (436.8 cm^{-1}) shown in Table V is close to this wavenumber. Hence, we interpret this broad peak as being due to the local vibrational mode of Ba$_{Si}$. To investigate the other two Raman peaks at around 560 and 590 cm^{-1} in Fig. 11, we measured the Raman spectrum at 78 K on the sample with $R_{Ba}/R_{Si} = 2.2$ as shown in Fig. 13(a). In the range between 560 and 600 cm^{-1}, three peaks appear at 561.3, 576.0, and 590.2 cm^{-1}. The wavenumbers 561.3 and 590.2 cm^{-1} almost double 279.8 and 296.6 cm^{-1}, respectively. Hence, there is a possibility that the second order vibrational modes were observed. However, this assumption is not valid because of the following reasons. Figure 13(b) shows the Raman spectra measured at 78 K on samples with different R_{Ba}/R_{Si} values. Note that the spectra were normalized using the peak intensity of the A$_g$ mode at 490 cm^{-1}. As shown in Fig. 13(b), the signal intensities in the range between 500 and 600 cm^{-1} are quite sensitive to R_{Ba}/R_{Si}, whereas there is not so much difference in the other range. Besides, they become higher as R_{Ba}/R_{Si} is deviated away from the vicinity of 2.2. These results suggest that the Raman peaks at around 560 and 590 cm^{-1} in Fig. 11 originate
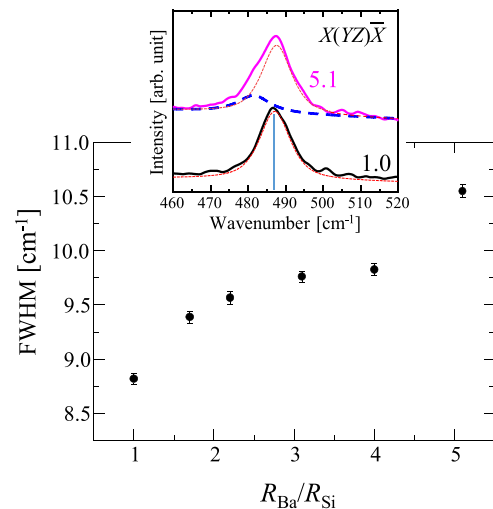

FIG. 9. A main peak (A$_g$ mode) position [shown in Fig. 8(a)] as a function of weighted N_{Ba}/N_{Si} for $R_{Ba}/R_{Si} = 1.0$, 2.2, and 4.0.

FIG. 10. FWHM values of the peak intensity at around 490 cm^{-1} as a function of R_{Ba}/R_{Si} at RT. Polarized Raman spectra measured at the $X(YZ)\overline{X}$ geometry on samples at $R_{Ba}/R_{Si} = 1.0$ and 5.1 are inserted.
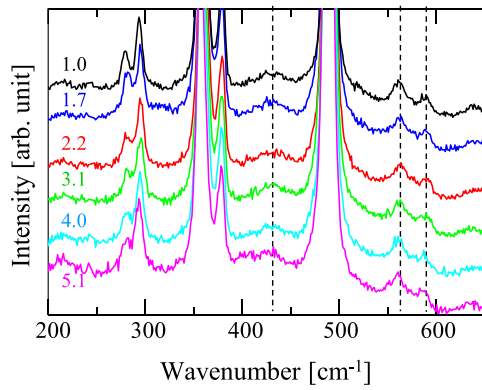
FIG. 11. Highlighted Raman spectra of BaSi$_2$ films with different R_{Ba}/R_{Si} values. Additional peaks are observed along the broken lines.

from defects. It is considered that Si$_i$ is considered one of the origins because the calculated phonon frequency of Si$_i$ (556.7 cm^{-1}) is close to 560 cm^{-1}. O$_i$ (597.3 cm^{-1}) is also a candidate because it is close to 590 cm^{-1}, and the oxygen concentration in BaSi$_2$ films grown by MBE is more than 10^{19} cm^{-3} according to Ref. 58. At present, we do not have sufficient data to discuss further. Thus, further studies are mandatory; however, we may reasonably conclude that Raman spectroscopy is an effective means to understand the presence of native point defects in BaSi$_2$.

IV. CONCLUSION

In this study, the residual stress in the *a*-axis-oriented BaSi$_2$ epitaxially films grown on Si(111) substrates was estimated by the lattice constants *a*, *b*, and *c* deduced from the measured XRD peak positions, and it was found that the native defects are responsible for the stress. Analysis of the vibrational frequency using Quantum Espresso indicates that the local vibrational modes of Ba$_{Si}$, V$_{Si}$, and Si$_i$ appear at around 430, 480, and 560 cm^{-1}, respectively, and the main Raman peak at around 490 cm^{-1} shifts to a lower wavenumber by the presence of these defects. Comparing the experimental results with the calculated ones, we observed peaks
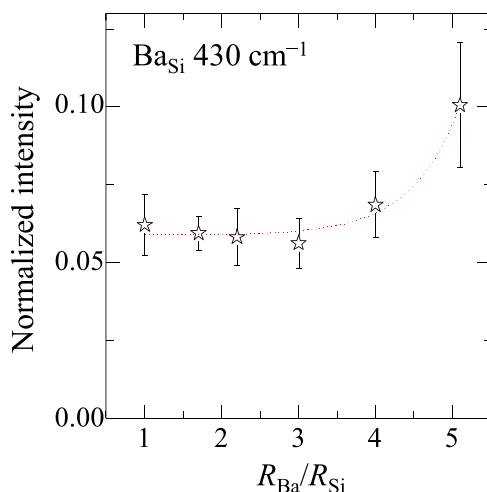

FIG. 12. R_{Ba}/R_{Si} dependence of the peak intensity at around 430 cm^{-1} normalized using the peak intensity of the Ag mode at around 490 cm^{-1}. The dotted lines are guides to the eye.
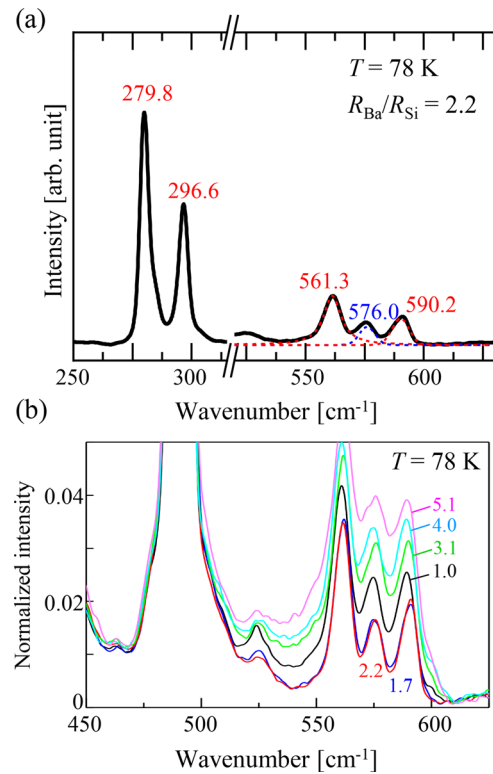

FIG. 13. (a) Raman spectrum of the sample with $R_{Ba}/R_{Si} = 2.2$ at 78 K. (b) Normalized Raman spectra of samples with different R_{Ba}/R_{Si} values at 78 K.

due to local vibrational modes of V$_{Si}$ and Ba$_{Si}$ and those probably caused by Si$_i$ and/or O$_i$.

[1]K. Yoshikawa, H. Kawasaki, W. Yoshida, T. Irie, K. Konishi, K. Nakano, T. Uto, D. Adachi, M. Kanematsu, H. Uzu, and K. Yamamoto, Nat. Energy **2**, 17032 (2017).
[2]W. Shockley and H. J. Queisser, J. Appl. Phys. **32**, 510 (1961).
[3]P. Jackson, R. Wuerz, D. Hariskos, E. Lotter, W. Witte, and M. Powalla, Phys. Status Solidi RRL **10**, 583 (2016).
[4]X. Wu, Sol. Energy **77**, 803 (2004).
[5]J. Burschka, N. Pellet, S.-J. Moon, R. Humphry-Baker, P. Gao, M. K. Nazeeruddin, and M. Grätzel, Nature **499**, 316 (2013).
[6]W. S. Yang, J. H. Noh, N. J. Jeon, Y. C. Kim, S. Ryu, J. Seo, and S. I. Seok, Science **348**, 1234 (2015).
[7]T. Suemasu and N. Usami, J. Phys. D: Appl. Phys. **50**, 023001 (2017).
[8]M. Baba, K. Toh, K. Toko, N. Saito, N. Yoshizawa, K. Jiptner, T. Sakiguchi, K. O. Hara, N. Usami, and T. Suemasu, J. Cryst. Growth **348**, 75 (2012).
[9]K. O. Hara, N. Usami, K. Toh, M. Baba, K. Toko, and T. Suemasu, J. Appl. Phys. **112**, 083108 (2012).
[10]K. O. Hara, N. Usami, K. Nakamura, R. Takabe, M. Baba, K. Toko, and T. Suemasu, Appl. Phys. Express **6**, 112302 (2013).
[11]R. Takabe, K. O. Hara, M. Baba, W. Du, N. Shimada, K. Toko, N. Usami, and T. Suemasu, J. Appl. Phys. **115**, 193510 (2014).
[12]K. Toh, T. Saito, and T. Suemasu, Jpn. J. Appl. Phys., Part 1 **50**, 068001 (2011).
[13]T. Nakamura, T. Suemasu, K. Takakura, and F. Hasegawa, Appl. Phys. Lett. **81**, 1032 (2002).
[14]D. B. Migas, V. L. Shaposhnikov, and V. E. Borisenko, Phys. Status Solidi B **244**, 2611 (2007).

[15]M. Kumar, N. Umezawa, and M. Imai, J. Appl. Phys. **115**, 203718 (2014).

[16]M. Kumar, N. Umezawa, and M. Imai, Appl. Phys. Express **7**, 071203 (2014).

[17]T. Suemasu, Jpn. J. Appl. Phys., Part 1 **54**, 07JA01 (2015).

[18]R. A. McKee and F. J. Walker, Appl. Phys. Lett. **63**, 2818 (1993).

[19]K. Morita, M. Kobayashi, and T. Suemasu, Jpn. J. Appl. Phys., Part 1 **45**, L390 (2006).

[20]Y. Imai and A. Watanabe, Intermetallics **18**, 1432 (2010).

[21]S. Yachi, R. Takabe, K. Toko, and T. Suemasu, Appl. Phys. Lett. **109**, 072103 (2016).

[22]T. Deng, T. Sato, Z. Xu, R. Takabe, S. Yachi, Y. Yamashita, K. Toko, and T. Suemasu, Appl. Phys. Express **11**, 062301 (2018).

[23]K. Kodama, R. Takabe, T. Deng, K. Toko, and T. Suemasu, Jpn. J. Appl. Phys. **57**, 058004 (2018).

[24]R. Takabe, K. Nakamura, M. Baba, W. Du, M. Ajmal Khan, K. Toko, M. Sasase, N. Usami, and T. Suemasu, Jpn. J. Appl. Phys., Part 1 **53**, 04ER04 (2014).

[25]Y. Nakagawa, K. O. Hara, T. Suemasu, and N. Usami, Jpn. J. Appl. Phys., Part 1 **54**, 08KC03 (2015).

[26]T. Yoneyama, A. Okada, M. Suzuno, T. Shibutami, K. Matsumaru, K. Toko, and T. Suemasu, Thin Solid Films **534**, 116 (2013).

[27]R. Takabe, T. Deng, K. Kodama, Y. Yamashita, T. Sato, K. Toko, and T. Suemasu, J. Appl. Phys. **123**, 045703 (2018).

[28]M. Kumar, N. Umezawa, W. Zhou, and M. Imai, J. Mater. Chem. A **5**, 25293 (2017).

[29]H. Takeuchi, W. Du, M. Baba, R. Takabe, K. Toko, and T. Suemasu, Jpn. J. Appl. Phys., Part 1 **54**, 07JE01 (2015).

[30]S. Yachi, R. Takabe, T. Deng, K. Toko, and T. Suemasu, Jpn. J. Appl. Phys., Part 1 **57**, 042301 (2018).

[31]Y. Yamashita, S. Yachi, R. Takabe, T. Sato, M. E. Bayu, K. Toko, and T. Suemasu, Jpn. J. Appl. Phys., Part 1 **57**, 025501 (2018).

[32]C. M. Ruiz, X. Fontané, A. Fairbrother, V. Izquierdo-Roca, C. Broussillou, S. Bodnar, A. Pérez-Rodríguez, and V. Bermúdez, Appl. Phys. Lett. **102**, 091106 (2013).

[33]M. Iinuma, H. Tsukamoto, N. Murakoso, H. Yamaguchi, and Y. Terai, JJAP Conf. Proc. **5**, 011106 (2017).

[34]M. Somer, Z. Anorg. Allg. Chem. **626**, 2478 (2000).

[35]H. Peng, C. L. Wang, J. C. Li, R. Z. Zhang, M. X. Wang, H. C. Wang, Y. Sun, and M. Sheng, Phys. Lett. A **374**, 3797 (2010).

[36]K. O. Hara, C. T. Trinh, K. Arimoto, J. Yamanaka, K. Nakagawa, Y. Kurokawa, T. Suemasu, and N. Usami, J. Appl. Phys. **120**, 045103 (2016).

[37]Y. Terai, H. Yamaguchi, H. Tsukamoto, N. Murakami, M. Iinuma, and T. Suemasu, Jpn. J. Appl. Phys., Part 1 **56**, 05DD02 (2017).

[38]Y. Inomata, T. Nakamura, T. Suemasu, and F. Hasegawa, Jpn. J. Appl. Phys., Part 1 **43**, 4155 (2004).

[39]R. Takabe, S. Yachi, W. Du, D. Tsukahara, H. Takeuchi, K. Toko, and T. Suemasu, AIP Adv. **6**, 085107 (2016).

[40]R. Takabe, H. Takeuchi, W. Du, K. Ito, K. Toko, S. Ueda, A. Kimura, and T. Suemasu, J. Appl. Phys. **119**, 165304 (2016).

[41]J. B. Nelson and D. P. Riley, Proc. Phys. Soc. **57**, 160 (1945).

[42]M. Diem, *Modern Vibrational Spectroscopy and Micro-Spectroscopy*, 1st ed. (John Wiley & Sons, Chichester, 2015), Chap. 4.2.

[43]D. Tsukahara, M. Baba, S. Honda, Y. Imai, K. O. Hara, N. Usami, K. Toko, J. H. Werner, and T. Suemasu, J. Appl. Phys. **116**, 123709 (2014).

[44]Y. Imai and A. Watanabe, Intermetallics **19**, 1102 (2011).

[45]P. Giannozzi, S. Baroni, N. Bonini, M. Calandra, R. Car, C. Cavazzoni, D. Ceresoli, G. L. Chiarotti, M. Cococcioni, I. Dabo, A. Dal Corso, S. de Gironcoli, S. Fabris, G. Fratesi, R. Gebauer, U. Gerstmann, C. Gougoussis, A. Kokalj, M. Lazzeri, L. Martin-Samos, N. Marzari, F. Mauri, R. Mazzarello, S. Paolini, A. Pasquarello, L. Paulatto, C. Sbraccia, S. Scandolo, G. Sclauzero, A. P. Seitsonen, A. Smogunov, P. Umari, and R. M. Wentzcovitch, J. Phys.: Condens. Matter **21**, 395502 (2009).

[46]S. Baroni, S. d Gironcoli, and P. Giannozzi, Rev. Mod. Phys. **73**, 515 (2001).

[47]We used Si.pbe-mt_fhi.UPF, Ba.pbe-mt_fhi.UPF, B.pbe-mt_fhi.UPF and Sb.pbe-mt_fhi.UPF from http://www.quantum-espresso.org.

[48]S. J. Fonash, J. Appl. Phys. **44**, 4607 (1973).

[49]C. H. Hsueha and S. Lee, Composites B **34**, 747 (2003).

[50]T. Goebel, Y. Prots, and F. Haarmann, Z. Kristallogr. NCS **224**, 7 (2009).

[51]M. F. Doerner and S. Brennan, J. Appl. Phys. **63**, 126 (1988).

[52]M. Imai, Jpn. J. Appl. Phys. **50**, 101801 (2011).

[53]H. S. Story and R. W. Hoffman, Proc. Phys. Soc. B **70**, 950 (1957).

[54]J. D. Finegan and R. W. Hoffman, J. Appl. Phys. **30**, 597 (1959).

[55]J. H. van der Merwe, Philos. Mag. **7**, 1433 (1962).

[56]C. P. Herrero and M. Stutzmann, Phys. Rev. B **38**, 12668 (1988).

[57]H. Schäfer, K. H. Janzou, and A. Weiss, Angew. Chem. Int. Ed. **2**, 393 (1963).

[58]W. Du, R. Takabe, S. Yachi, K. Toko, and T. Suemasu, Thin Solid Films **629**, 17 (2017).